

---

# Spectrally-Guided Diffusion Noise Schedules

---

Carlos Esteves<sup>1</sup> Ameesh Makadia<sup>1</sup>

## Abstract

Denosing diffusion models are widely used for high-quality image and video generation. Their performance depends on noise schedules, which define the distribution of noise levels applied during training and the sequence of noise levels traversed during sampling. Noise schedules are typically handcrafted and require manual tuning across different resolutions. In this work, we propose a principled way to design per-instance noise schedules for pixel diffusion, based on the image’s spectral properties. By deriving theoretical bounds on the efficacy of minimum and maximum noise levels, we design “tight” noise schedules that eliminate redundant steps. During inference, we propose to conditionally sample such noise schedules. Experiments show that our noise schedules improve generative quality of single-stage pixel diffusion models, particularly in the low-step regime.

## 1. Introduction

Denosing diffusion models (Sohl-Dickstein et al., 2015; Ho et al., 2020) are generative models based on learning to reverse a noising process that progressively destroys the data. They are the foundation of state-of-the-art media generation since Latent Diffusion Models (LDM) (Rombach et al., 2022), which operate on the latent space of a visual autoencoder. This combination produced a series of popular applications on image (Ramesh et al., 2025; Podell et al., 2024) and video generation (Blattmann et al., 2023; Brooks et al., 2024; DeepMind, 2025).

Despite the LDM dominance, they have disadvantages – the generation quality is inherently capped by the autoencoder/tokenizer quality, and the two-stage training can be cumbersome, since there is no clear connection between the autoencoder reconstruction and generative performance (Yu et al., 2024; Hansen-Estruch et al., 2025). Some alternatives avoid generation on latent space but still require multi-stage

training for upsampling in pixel space (Nichol & Dhariwal, 2021; Ho et al., 2022; Saharia et al., 2022).

These disadvantages motivated recent renovations in single-stage pixel diffusion (Hoogeboom et al., 2023; 2025; Chen et al., 2025; Wang et al., 2025; Li & He, 2025; Yu et al., 2025), with improvements in model architecture and training protocol reducing the gap to LDMs. While significant progress has been made, LDMs still show better generative quality at lower computational cost. One of the reasons is that LDMs require up to one order of magnitude fewer denoising steps than pixel diffusion (Hoogeboom et al., 2025).

The noise level of each denoising step is determined by the *noise schedule*, which is typically handcrafted as a linear or cosine-like curve increasing with the time step  $t$ . Recent approaches such as Simple Diffusion (Hoogeboom et al., 2023) adapt the schedule across resolutions by shifting the curve. As illustrated in Fig. 2 (left), these heuristics relate to the power spectrum observed in natural images – higher resolution images have more energy at lower frequencies, thus more noise is needed to destroy the signal. Since following these dataset-level spectral trends with heuristics has been successful, we posit that adapting the schedule to the spectrum of each instance can provide further improvements.

In this work, we observe that typical noise schedules are inefficient, prescribing inappropriate noise levels for a significant number of steps (see Fig. 1). We design a principled noise schedule that adapts to each image based on its spectral properties, and show that it improves quality with significantly less deterioration under reduced number of denoising steps.

Our contributions are as follows. 1) We design “tight” per-instance noise schedules that follow the signal’s power spectrum. 2) We derive theoretical bounds on the efficacy of minimum and maximum noise levels. 3) We propose a conditional mechanism to predict the power spectrum and corresponding noise schedule prior to image sampling. 4) We demonstrate that our schedules improve generative quality compared to baseline pixel diffusion models, with particularly large margins in the low-step regime.

<sup>1</sup>Google Research. Correspondence to: Carlos Esteves <machc@google.com>.

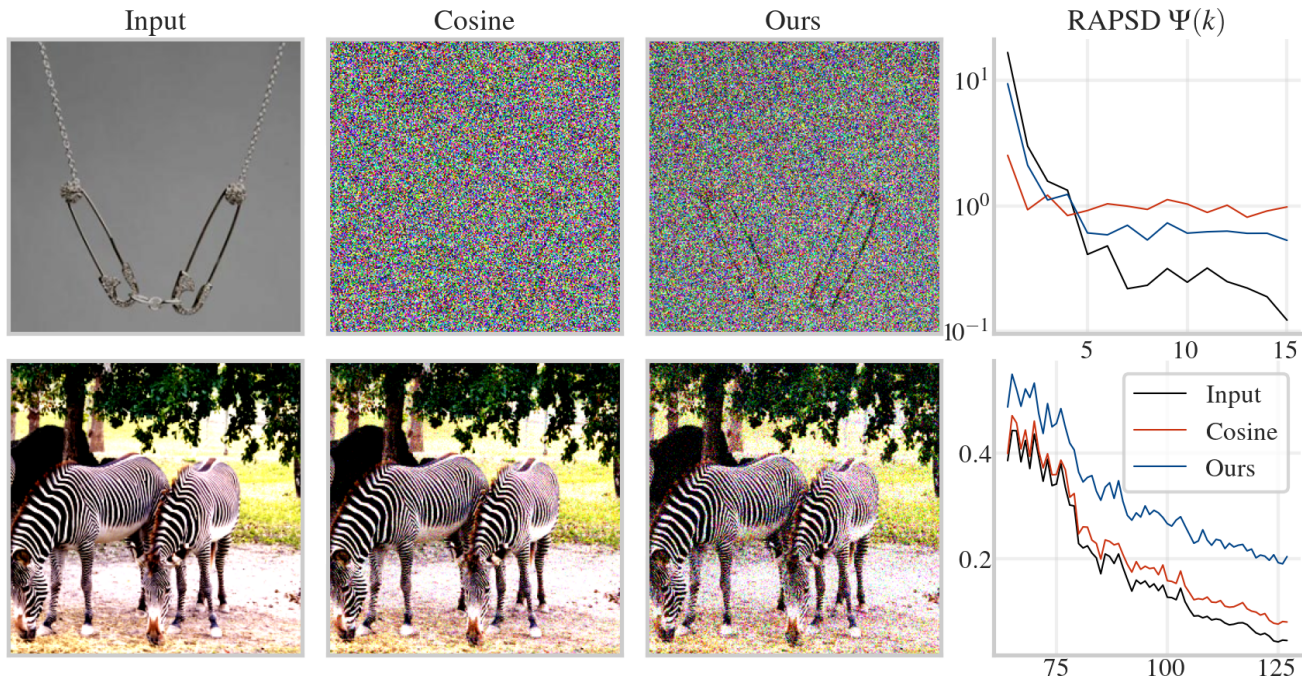


Figure 1. Our “tight” schedules adapt to each instance’s spectrum, ensuring effective noise levels at all steps. *Top*: An image with low energy on low frequencies. The standard cosine noise schedule destroys the signal at  $t = 0.5$ , which means that at least half of the training steps would apply excessive noise for this input. Our adaptive schedule preserves the low frequency content – notice that the object outline is still visible. *Bottom*: An image with high energy on high frequencies. The cosine schedule barely changes the input at  $t = 0.1$  – notice that the RAPSD curves between the cosine schedule and the input are close and correlated. This means that at least 10% of the training steps would apply insufficient noise. Our schedule is effective at destroying a part of the high-frequency content at this level.

## 2. Related work

**Diffusion models** were introduced by Sohl-Dickstein et al. (2015) and received increased attention in media generation since DDPM (Ho et al., 2020). Rombach et al. (2022) laid out the core ideas for current state-of-the-art LDMs. Here we depart from LDMs and adopt pixel diffusion, closely following the formulation of VDM++ (Kingma et al., 2021; Kingma & Gao, 2023) and the architectures and protocols of Simpler Diffusion (Hoogeboom et al., 2023; 2025).

**The noise schedule** is a crucial component of diffusion models and determines the noise level during training and sampling. Ho et al. (2020) adopted  $x_t = \sqrt{1 - \beta_t}x_{t-1} + \beta_t\epsilon$ , where  $\beta_t$  increased linearly with the time step and  $\epsilon \sim \mathcal{N}(0, I)$ . Nichol & Dhariwal (2021) introduced the widely used cosine schedule,  $x_t = \sqrt{\alpha_t}x_0 + \sqrt{1 - \alpha_t}\epsilon$ , where  $\alpha_t$  decays little near  $t = 0$  and  $t = 1$  and linearly in the middle. EDM (Karras et al., 2022) established a log-normal distribution of noise levels to prioritize intermediate levels. Hang et al. (2025) connected the noise schedules with importance sampling of logSNR and verified importance of intermediate levels (zero logSNR). Lin et al. (2024) corrected a number of flaws identified in diffusion implementations. Esser et al. (2024) extended Kingma & Gao (2023) analysis to rectified flows (Liu et al., 2022; Albergo & Vanden-Eijnden, 2023; Lipman et al., 2023) and again found it best to prioritize

intermediate noise levels. These methods prescribe a global noise schedule, while ours is different for each instance.

**Noise schedules across resolutions** Jabri et al. (2023) introduced the sigmoid schedule with temperature that downweights extreme noise levels; they also noticed that increasing the temperature shifts the schedule towards more noise and performs better at higher resolution. Chen (2023) suggested a simple idea of scaling inputs by a constant factor to adjust the noise factor so that more noise can be introduced for higher resolutions. Hoogeboom et al. (2023) observed directly that more noise is needed to destroy high-resolution signals, and proposed to shift the noise schedule according to the input resolution. They further proposed a timestep dependent shift that happens at low signal-to-noise ratio (SNR) and not high. These design decisions relate to the power spectrum trends depicted in Fig. 2 (left); the power at lower frequencies increases with the image resolution, which also introduces new low-powered high frequencies, justifying the timestep-dependent shifts. In this work, we explicitly use each instance’s power spectrum to determine its noise schedule; in aggregate this gives rise to similar trends as prior work (see Fig. 2), but our schedules naturally adapt to each instance and resolution without handcrafting.

**Learning noise schedules** Kingma et al. (2021) showed that, in theory, the noise schedule does not matter since the

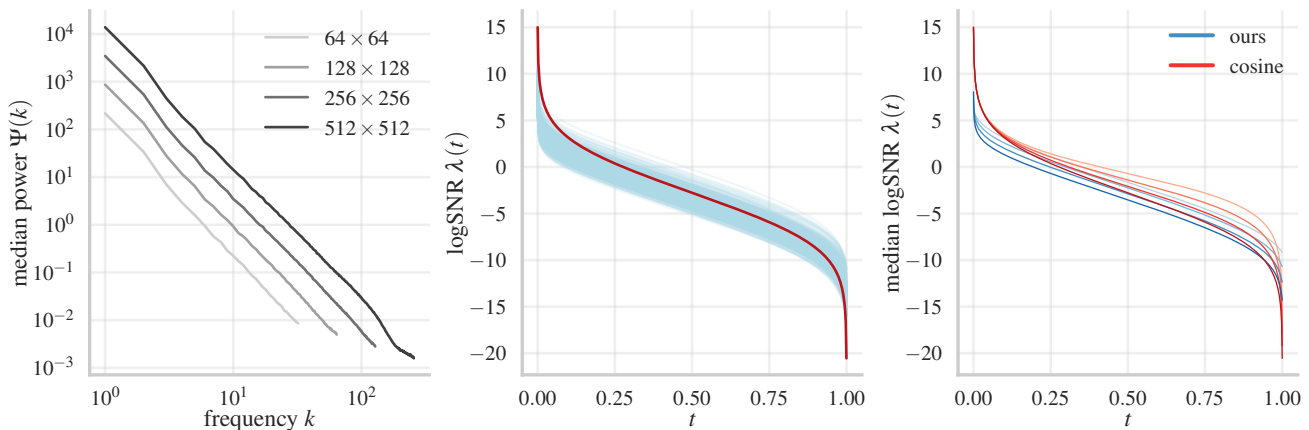


Figure 2. Our noise schedules vary per instance based on its spectral properties. *Left*: Median power per frequency for ImageNet at multiple resolutions (increasing from light to dark). The power spectrum of natural images follows a power law whose trends explain current noise schedule tuning heuristics. We eschew such heuristics and use each instance spectrum to determine its schedule. *Middle*: Cosine schedule and ours for 1000 images from ImageNet  $256 \times 256$ . *Right*: Median noise schedules for the same set of images, at  $128 \times 128$ ,  $256 \times 256$ , and  $512 \times 512$  (light to dark color). Our schedules avoid excessively high and low noise values, while following similar trends to the baseline across resolutions without any hyperparameter change.

loss reduces to an integral between minimum and maximum SNR. Kingma & Gao (2023) observed that, in practice, the schedule affects the variance of the Monte-Carlo estimation of the loss which in turn affects optimization efficiency. They proposed an adaptive noise schedule based on the training loss, which resulted similar quality but potentially faster training. Sahoo et al. (2024) learned a per-pixel polynomial noise schedule that optimizes a tighter evidence lower bound (ELBO), with a focus on improving density estimation. Our method is simpler, connecting the noise schedule to each instance’s spectral properties, while showing clear improvements in quality and denoising steps reduction.

**Spectral analysis and diffusion models** There is growing literature in understanding diffusion through the lens of spectral analysis. Rissanen et al. (2023); Dieleman (2024) connected diffusion with spectral autoregression, as both processes generate images by progressively introducing frequencies. Falck et al. (2025) showed evidence against this interpretation and introduced EqualSNR to enforce that all frequencies are corrupted equally during the forward process, achieving similar quality. Huang et al. (2024) found improvements by using blue instead of white noise. Jiralerspong et al. (2025) showed improvements by designing colored noise with more power on low-frequencies than high. Based on spectral analysis of the denoising process of Gaussian-generated data with arbitrary covariance, Benita et al. (2025) optimized a noise schedule end-to-end for a given dataset, resolution, and number of sampling steps. The optimized schedules followed similar trends to handcrafted cosine. These references still prescribed noise schedules for a whole dataset, while we propose a per-instance strategy that adapts to the spectral diversity within the dataset.

**Reducing the number of denoising steps** Diffusion modeling in latent space (Rombach et al., 2022) naturally requires fewer denoising steps than in higher dimensional pixel space. Distillation is a popular strategy for step count reduction (Song et al., 2023; Salimans & Ho, 2022; Yin et al., 2024; Nguyen & Tran, 2024; Meng et al., 2023; Salimans et al., 2024). Another class of techniques are rectified flows (Liu et al., 2022; Albergo & Vanden-Eijnden, 2023; Lipman et al., 2023; Lee et al., 2024), and mean flows (Geng et al., 2025). These are complementary to our per-instance noise schedules, and could potentially be combined.

### 3. Background

The forward time diffusion process is given by

$$x_t = \alpha_t x_0 + \sigma_t \epsilon, \quad \epsilon \sim \mathcal{N}(0, I), \quad 0 \leq t \leq 1, \quad (1)$$

where  $x_0$  is a clean image. The noise schedule determines  $\alpha_t$  and  $\sigma_t$ ; for example,  $\alpha_t = \cos(\pi t/2)$  defines a cosine schedule. Schedules are often defined in terms of the logSNR  $\lambda(t) = \log(\alpha_t^2/\sigma_t^2)$  (Kingma et al., 2021).

During training, we minimize the sigmoid-weighted ELBO, following Kingma & Gao (2023); Hoozeboom et al. (2025).

$$\mathcal{L}_\theta(x_0; t, y) = -\lambda'(t) e^b \sigma(\lambda(t) - b) \|x_\theta(x_t; c) - x_0\|_2^2, \quad (2)$$

where  $t \sim \mathcal{U}(0, 1)$ ,  $b$  is a constant bias,  $\sigma$  is the sigmoid function, and  $x_\theta$  is a neural network. A typical conditioning is  $c = (t, y)$ , where  $y$  is the class label or text prompt. After

**Algorithm 1** Training with Spectrally-Guided Schedules

**Input:** Dataset  $\mathcal{D}$ , model  $x_\theta$   
**for**  $i = 1$  **to** num\_steps **do**  
 Sample data  $x_0 \sim \mathcal{D}$  with label/prompt  $y$   
 Sample time  $t \sim \mathcal{U}(0, 1)$  and noise  $\epsilon \sim \mathcal{N}(0, I)$   
 Compute RAPSD  $\Psi_{x_0}$  from  $x_0$   $\triangleright$  Eqs. (6) and (7)  
 Fit  $\tilde{\Psi}_{x_0}(k) = \beta k^\alpha$  to  $\Psi_{x_0}$   $\triangleright$  Section 4.4  
 Compute schedule  $\lambda_M$  using  $\tilde{\Psi}_{x_0}$   $\triangleright$  Eqs. (17) to (21)  
 Compute  $\alpha_t, \sigma_t$ , and  $x_t$  using  $\lambda_M$   $\triangleright$  Eqs. (1) and (15)  
 Update params  $\theta$  given  $\nabla_\theta \mathcal{L}$  over a batch  $\triangleright$  Eq. (2)  
**end for**

training, we use ancestral sampling for generation,

$$\hat{x}_\theta = x_\theta(x_t; c) + w(x_\theta(x_t; c) - x_\theta(x_t; c_\theta)), \quad (3)$$

$$x_s = \alpha_s \hat{x}_\theta + \frac{\alpha_t \sigma_s^2}{\alpha_s \sigma_t^2} (x_t - \alpha_t \hat{x}_\theta) + \sigma_{t \rightarrow s} \epsilon, \quad (4)$$

$$\sigma_{t \rightarrow s} = \sigma_s^{1-\gamma} \sigma_t^\gamma \sqrt{1 - \exp(\lambda(t) - \lambda(s))}, \quad (5)$$

where  $w$  is the scale of classifier-free guidance (Ho & Salimans, 2021),  $c_\theta$  is the conditioning with a null label/prompt embedding,  $s < t$  and  $\gamma$  is a hyperparameter. This process starts from pure noise and is repeated until  $s = 0$ .

## 4. Method

### 4.1. Preliminaries

Consider a discrete signal  $x : \{0, \dots, N-1\}^d \rightarrow \mathbb{R}$ . Its Discrete Fourier Transform (DFT) is,

$$\hat{x}(u) = \frac{1}{N^{d/2}} \sum_n x(n) \exp\left(-i \frac{2\pi}{N} u^\top n\right). \quad (6)$$

The power spectral density is  $P_x(u) = |\hat{x}(u)|^2$ . The radially-averaged power spectral density (RAPSD)

$$\Psi_x(k) = \frac{1}{N_k} \sum_{u: \text{round}(\|u\|_2)=k} P_x(u), \quad (7)$$

where  $k = \|u\|_2$  is the scalar frequency, and  $N_k$  the number of frequency vectors  $u$  that satisfy the rounding. In this work, we focus on RGB images so  $\Psi_x(k) = 1/3 \sum_{c=1}^3 \Psi_{x_c}(k)$ , where  $c$  indexes the color channels, and  $0 \leq k \leq N_f$ , with  $N_f$  being the Nyquist frequency (half of the image side).

For natural images, ignoring the DC component  $u = \mathbf{0}$  so  $k \geq 1$ , the RAPSD typically follows a power law,

$$\Psi_x(k) \approx k^\alpha \beta, \quad (8)$$

where  $\alpha < 0$  and  $\beta > 0$ . Furthermore,  $\alpha \approx -2$  and for range  $[-1, 1]$ ,  $\Psi_x(1) \gg 1$  and  $\Psi_x(N_f) \ll 1$  (Field, 1987; van der Schaaf & van Hateren, 1996; Torralba & Oliva, 2003). The RAPSD of white noise is one everywhere.

**Algorithm 2** Spectrally-Guided Sampling

**Input:** Label/prompt  $y$ , number of steps  $N$ .  
 Sample  $\alpha, \beta$  from  $S(y)$   $\triangleright$  Eqs. (22) to (24)  
 Define spectrum  $\tilde{\Psi}_x(k) = \beta k^\alpha$   
 Compute schedule  $\lambda_M$  using  $\tilde{\Psi}_x$   $\triangleright$  Eqs. (17) to (21)  
 Sample  $x_1 \sim \mathcal{N}(0, I)$   
**for**  $i = N$  **to** 1 **do**  
    $t \leftarrow i/N, \quad s \leftarrow (i-1)/N$   
   Compute  $\alpha_t, \sigma_t, \alpha_s, \sigma_s$  from  $\lambda_M$   $\triangleright$  Eq. (15)  
   Get  $x_s$  from  $x_t$  given  $\epsilon \sim \mathcal{N}(0, I)$   $\triangleright$  Eqs. (3) to (5)  
**end for**  
**Return**  $x_0$

### 4.2. Noise level per frequency

Our main contribution is a per-instance noise schedule that follows the power spectrum, avoiding too much or too little noise. This amounts to prescribing 1) the minimum amount of noise that destroys the signal, 2) the maximum amount of noise that preserves the signal, and 3) everything in between.

At some noise level  $q$ , we obtain the RAPSD of the noised input  $z_q = \alpha_q x_0 + \sigma_q \epsilon$  as (see proof in Section A),

$$\Psi_{z_q}(k) = \alpha_q^2 \Psi_{x_0}(k) + \sigma_q^2. \quad (9)$$

Suppose we set the noise level  $\sigma_q$  proportional to the power at some frequency  $q$ , with  $\kappa_q > 0$ ,

$$\sigma_q^2 = \kappa_q \alpha_q^2 \Psi_{x_0}(q). \quad (10)$$

Substituting Eq. (10) into Eq. (9) and assuming a variance-preserving schedule,  $\alpha_q^2 + \sigma_q^2 = 1$ , we have, for all  $k$ ,

$$\Psi_{z_q}(k) = \frac{\Psi_{x_0}(k) + \kappa_q \Psi_{x_0}(q)}{1 + \kappa_q \Psi_{x_0}(q)}. \quad (11)$$

**Largest noise** For  $q = 1$  we have  $\Psi_{x_0}(q) \gg 1$ . Thus,

$$\Psi_{z_1}(k) \approx \frac{\Psi_{x_0}(k) + \kappa_1 \Psi_{x_0}(1)}{\kappa_1 \Psi_{x_0}(1)} = 1 + \frac{\Psi_{x_0}(k)}{\kappa_1 \Psi_{x_0}(1)}. \quad (12)$$

For  $k = 1$ , we have  $\Psi_{z_1}(1) \approx 1 + 1/\kappa_1$ , while for  $k > 1$  we have  $\Psi_{x_0}(k) \lesssim \Psi_{x_0}(1)$  and  $\Psi_{z_1}(k) \lesssim 1 + 1/\kappa_1$ .<sup>1</sup> Since  $\Psi_{z_1}(k) \lesssim 1 + 1/\kappa_1$  holds for all  $k$ , the greater  $\kappa_1$  is, the closer the RAPSD is to the one of unit Gaussian noise. This measures how close the signal is to pure noise, and determines our maximum noise level. We define  $\kappa_{\max} = \kappa_1$ .

**Smallest noise** For  $q = N_f$ ,  $\Psi_{x_0}(q) \ll 1$ . From Eq. (11),

$$\Psi_{z_{N_f}}(k) \approx \Psi_{x_0}(k) + \kappa_{N_f} \Psi_{x_0}(N_f) \quad (13)$$

<sup>1</sup>Typically  $\Psi_{x_0}$  is monotonically decreasing so  $\Psi_{x_0}(k) < \Psi_{x_0}(1)$  and  $\Psi_{z_1}(k) < 1 + 1/\kappa_1$ . We ensure this in Section 4.4.

## Spectrally-Guided Diffusion Noise Schedules

Table 1. Class-conditional generation on ImageNet. We compare our spectral noise scheduling against recent single-stage pixel diffusion baselines. The fairest comparison is against SiD2 (Hoogeboom et al., 2025); we use exactly the same architecture and training protocol except for our contributions described in Section 4. We outperform the baselines in most metrics, while needing fewer denoising steps than SiD2. SiD2 only reported FIDs. We reproduce it and compute additional metrics; originally reported results are quoted next to reproduced. Ours and SiD2 values are averaged over 5 sets of generations with different seeds. **NFE**: number of function evaluations (denoising steps). **Adapt.**: PixelFlow uses a (slower) solver with adaptive number of steps.

MODEL	PARAMS	NFE	FID ↓	SFID ↓	IS ↑	PRECISION ↑	RECALL ↑
<b>IMAGENET 512 × 512</b>							
JIT-G (LI & HE, 2025)	2B	-	1.78	-	306.8	-	-
PIXNERD-XL/16 (WANG ET AL., 2025)	700M	100	2.84	5.95	245.6	<b>0.80</b>	0.59
SID2, SMALL	397M	512	2.19 (2.19)	4.30	295.3	0.72	0.63
<b>OURS, SMALL</b>	399M	256	1.79	4.39	306.1	0.73	<b>0.64</b>
SID2, FLOP HEAVY	397M	512	1.53 (1.48)	3.98	306.2	0.74	0.63
<b>OURS, FLOP HEAVY</b>	399M	320	<b>1.45</b>	<b>3.91</b>	<b>310.0</b>	0.74	0.63
<b>IMAGENET 256 × 256</b>							
JIT-G (LI & HE, 2025)	2B	-	1.82	-	292.6	0.79	0.62
PIXELFLOW-XL (CHEN ET AL., 2025)	677M	ADAPT.	1.98	5.83	282.1	<b>0.81</b>	0.60
PIXNERD-XL/16 (WANG ET AL., 2025)	700M	100	2.15	4.55	<b>297.0</b>	0.79	0.59
PIXELDIT-XL (YU ET AL., 2025)	797M	100	1.61	4.68	292.7	0.78	0.64
SID2, SMALL	397M	512	1.68 (1.72)	4.04	288.2	0.72	<b>0.65</b>
<b>OURS, SMALL</b>	399M	256	1.42	3.82	<b>297.0</b>	0.73	<b>0.65</b>
SID2, FLOP HEAVY	397M	512	1.37 (1.38)	3.83	286.3	0.73	<b>0.65</b>
<b>OURS, FLOP HEAVY</b>	399M	256	<b>1.32</b>	<b>3.71</b>	294.2	0.74	0.64
<b>IMAGENET 128 × 128</b>							
SID2, SMALL	397M	512	1.62	3.76	220.0	0.73	0.64
<b>OURS, SMALL</b>	399M	160	1.43	3.65	<b>223.9</b>	<b>0.74</b>	0.64
SID2, FLOP HEAVY	393M	512	1.30(1.26)	3.64	210.9	0.73	<b>0.65</b>
<b>OURS, FLOP HEAVY</b>	395M	160	1.30	<b>3.53</b>	204.8	0.73	0.64

Now for  $k = N_f$ , we have  $\Psi_{z_{N_f}}(N_f)/\Psi_{x_0}(N_f) \approx 1 + \kappa_{N_f}$ , while for  $k < N_f$  we have  $\Psi_{x_0}(k) \gtrsim \Psi_{x_0}(N_f)$  and  $\Psi_{z_{N_f}}(k)/\Psi_{x_0}(k) \lesssim 1 + \kappa_{N_f}$ . Thus, the smaller  $\kappa_{N_f}$  is, the closer the RAPSD of  $z_{N_f}$  is to the one of  $x$ ; this determines our minimum noise level. We define  $\kappa_{\min} = \kappa_{N_f}$ .

**In-between noise** Since there are several orders of magnitude between  $\kappa_{\max}$  and  $\kappa_{\min}$  (for example, for 1% tolerance we have  $\kappa_{\max} = 100$  and  $\kappa_{\min} = 0.01$ ), we prescribe the noise level at any frequency  $q$  by interpolating in log-space,

$$\kappa_q = \kappa_{\max}^{\frac{N_f - q}{N_f - 1}} \kappa_{\min}^{\frac{q - 1}{N_f - 1}}. \quad (14)$$

### 4.3. Noise schedule

Last section showed appropriate noise levels for each discrete frequency of the signal. Here we find the continuous monotonic noise schedule in terms of  $\lambda(t) = \log \alpha_t^2 / \sigma_t^2$ , with  $t \in [0, 1]$ . Under the variance-preserving assumption,

$$\alpha_t = \sqrt{\sigma(\lambda(t))}, \quad \sigma_t = \sqrt{\sigma(-\lambda(t))}. \quad (15)$$

We define  $\tilde{\Psi}_{x_0} : \mathbb{R} \rightarrow \mathbb{R}$  as a monotonic continuous approximation of  $\Psi_{x_0}$ , and  $\kappa_t = \kappa_{\max}^t \kappa_{\min}^{1-t}$ . Now we need to map between  $t \in [0, 1]$  and  $q \in [1, N_f]$ .

**Frequency-focused schedule** The simplest such map is linear,  $\mu_F(t) = N_f + (1 - N_f)t$ , which yields the schedule,

$$\sigma_t^2 = \kappa_t \alpha_t^2 \tilde{\Psi}_{x_0}(\mu_F(t)), \quad (16)$$

$$\lambda_F(t; x_0) = -\log \kappa_t - \log \tilde{\Psi}_{x_0}(\mu_F(t)), \quad (17)$$

where Eq. (17) comes from computing the logSNR in Eq. (16). We denote  $\lambda_F$  the *frequency-focused* schedule, because, since  $t$  is sampled uniformly, the noise corresponding to each frequency appears at the same rate. Since most of the frequencies have low power, noise levels are low, focusing more on image details than on its coarse structure.

**Power-focused schedule** We propose an alternative map, where we use  $\tilde{\Psi}_{x_0}$  as a probability distribution function (PDF). Since power is concentrated in lower frequencies, this will cover higher noise levels more often, focusing more on coarse image structure than on high frequency details.

Let  $Z = \int_1^{N_f} \tilde{\Psi}_{x_0}(u) du$  be the normalization constant. We define the cumulative distribution function (CDF)  $F_{x_0}$  and

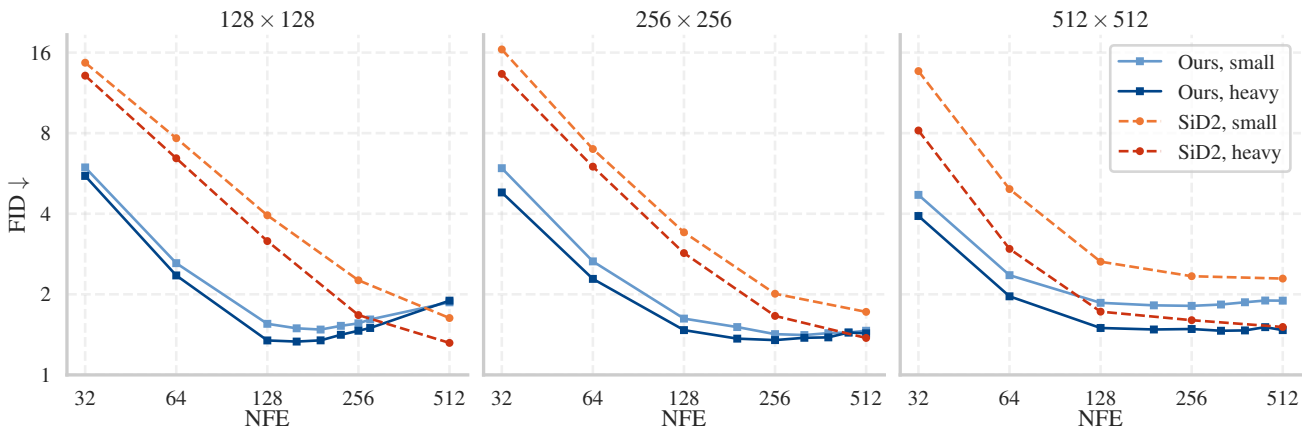


Figure 3. Comparison against the SiD2 (Hooeboom et al., 2025) baseline on ImageNet, at different number of function evaluations (NFE), or denoising steps. Our model outperforms the baseline at the optimal number of steps, and the gap widens as the number of steps reduces. Interestingly, our “tight” schedules exhibit a slight FID worsening at high number of steps.

the *power-focused* schedule  $\lambda_P$  as follows,

$$F_{x_0}(q) = \frac{1}{Z} \int_1^q \tilde{\Psi}_{x_0}(u) du, \quad (18)$$

$$\mu_P(t; x_0) = F_{x_0}^{-1}(1 - t), \quad (19)$$

$$\lambda_P(t; x_0) = -\log \kappa_t - \log \tilde{\Psi}_{x_0}(\mu_P(t; x_0)). \quad (20)$$

**Mixed schedule** To generate high quality images, the model needs to focus on both coarse structure and details. We found that combining the frequency and power-focused schedules achieves these goals and results in the best performance. We define the *mixed* schedule  $\lambda_M$  as, simply,

$$\lambda_M(t; x_0) = \frac{1}{2}(\lambda_F(t; x_0) + \lambda_P(t; x_0)). \quad (21)$$

Figure 2 shows this schedule, compared with the SiD (Hooeboom et al., 2023; 2025) baselines. The baseline schedules set a different shift for each resolution, while ours show similar trends across resolutions without any change.

#### 4.4. Fitting and sampling the power spectrum

The schedules defined in Section 4.3 come from each image during training time, by computing its RAPSD. However, they are not available during sampling, when the model generates an image given only the conditioning. Our solution is to sample the RAPSD before generating the image.

We approximate the RAPSD as a power-law  $\tilde{\Psi}_{x_0}(k) = k^\alpha \beta$  in order to 1) reduce the number of parameters to only two ( $\alpha$  and  $\beta$ ), and 2) ensure monotonicity. This is easily computed with least-squares in log-space, and enables finding closed-form equations for our schedules, see Section B.

We train an RAPSD sampler  $S$  that maps  $y$  (e.g. class label) to the parameters of a Gaussian Mixture Model (GMM) of  $C$  components: weights  $w_c$ , 2D means  $\mu_c$  and 2D diagonal

covariances  $\sigma_c$ . A simple linear layer works as this map for class-conditional generation and there is little difference between RAPSD sampler configurations and between using the sampler or the ground truth (see Section 5.4). We minimize the log-likelihood via stochastic gradient descent, which would also apply to other conditioning such as a text embedding. Now, before sampling from the diffusion model, we sample  $\alpha$  and  $\beta$  and proceed as usual. Formally,

$$\{w_c, \mu_c, \sigma_c\}_{c=1}^C = S(y), \quad (22)$$

$$c' \sim \text{Cat}(w_{1:C}), \quad \{v_1, v_2\} \sim \mathcal{N}(\mu_{c'}, \text{diag}(\sigma_{c'})), \quad (23)$$

$$\beta = \exp(v_1), \quad \alpha = \frac{v_2 - v_1}{\log N_f}, \quad (24)$$

where Cat is a categorical distribution. See also Section D.2.

#### 4.5. Conditioning and guidance interval

Our noise schedules require only two minor modifications to SiD2 (Hooeboom et al., 2025) for maximum performance. The baseline conditions the denoiser on the logSNR using FiLM (Perez et al., 2018), so it is aware of the noise level. Since we have a different noise schedule for each image, more information is needed to fully determine the schedule. We also condition on minimum and maximum logSNR per image, making  $c = (y, \lambda_M(t; x_0), \lambda_M(0; x_0), \lambda_M(1; x_0))$  in Eqs. (2) and (3). SiD2 defined the classifier-free guidance interval (Kynkäänniemi et al., 2024) in terms of logSNR, whereas, for similar reasons, we define it based on  $t$ . Section 5.4 shows the effect of these changes. Algorithms 1 and 2 summarize our training and sampling methods.

## 5. Experiments

We experiment on class-conditional image generation on ImageNet at multiple resolutions, closely following the architecture and training protocol defined in SiD2 (Hooeboom



Figure 4. Samples from ImageNet  $256 \times 256$ . Each  $2 \times 4$  block shows the SiD2 baseline on top and ours on bottom, while the number of denoising steps is, from left to right, 32, 64, 128, and 256. Our generations are noticeably of higher quality at low step counts.

et al., 2025). Section D reports implementation details.

### 5.1. Class-conditional image generation

Table 1 shows our results on class-conditional generation on ImageNet, and Figure 6 shows generated samples. We focus on comparisons with single-stage pixel diffusion models, excluding LDM and distilled models. The fairest comparison is against SiD2, which we reproduce and outperform in almost all metrics, while using fewer denoising steps, though the margin is smaller in the compute-heavy setting. Ours and SiD2 metrics are averaged over 5 runs.

While our results are strong in the single-stage pixel diffusion setting, they still do not reach the best LDMs and distilled models. As examples, RAE (Zheng et al., 2025) is an LDM that reach 1.13 FID on ImageNet with 50 denoising steps, and the distilled version of SiD2 achieves 1.50 FID on ImageNet  $512 \times 512$  with only 16 denoising steps.

### 5.2. Reducing the number of denoising steps

Our “tight” noise schedules significantly outperform the baselines in the low-step regime. Figure 3 shows the FID at varying number of denoising steps. Interestingly, our noise schedules exhibit a slight worsening at high-step counts so there is an optimal count for each resolution. Our model outperforms the baseline at the optimal count, and the gap widens at lower counts. Figure 4 compares generations.

### 5.3. Manipulating the sampled spectrum

We manipulate the sampled spectrum to modify properties of the generated image. For example, we can multiply the approximated RAPSD by a constant factor to change the contrast (since the power in spectral domain corresponds to variance in spatial). Here, we evaluate a more interesting manipulation, where we modify the RAPSD power law exponent ( $\alpha$  in Eq. (8)) such that the energy at the highest frequency changes by some factor. The effect enables controlling the amount of details of the generated image. This works because our model sees a number of different spectrum-based noise schedules during training and is conditioned on their parameters. Figure 5 shows some examples.

### 5.4. Ablations

Here we evaluate the effect of our architectural changes with respect to SiD2, as well as alternative designs that could be considered. Table 2 shows the results. Section C shows extra ablations on the hyperparameters we introduce; namely,  $\kappa_{\min}$ ,  $\kappa_{\max}$ , and the  $t$ -based guidance interval.

**Fixed schedule (median)** Typical noise schedules are the same for all images; here we quantify the effect of varying them per-instance. We adopt the same principles from Section 4.3, but make the schedule constant by taking the median schedule over a subset of training images. While this outperforms the SiD2 baseline, it underperforms ours.



Figure 5. Manipulating the sampled spectrum to modify generated image properties. Here we modify the sampled spectrum such that the energy at the highest frequency is multiplied by factors 0.1, 0.2, 0.4, 1.0, 2.5, 5.0, 10.0, respectively. This affects the noise schedule and the model conditioning, so it is a way to guide the model towards different spectral properties. In this example, the energy on high frequencies correlate to the amount of texture and details. Notice how the amount of details increase from left to right. Images are generated by the same model trained on ImageNet  $256 \times 256$  and same initial noise.

**Cosine MinMax** We evaluate the effect of using the RAPSD curves to guide the noise schedules. We use the prescriptions for minimum and maximum noise from Section 4.2 to design a per-instance schedule that follows a cosine between the extremes. It performs worse than ours.

**Frequency/Power focused** Our best noise schedule is an average of the frequency and power-focused schedules. Here we evaluate each of them independently.

**No conditioning** The only architectural modification we propose to SiD2 is the extra FiLM conditioning layers described in Section 4.5. Performance worsens without it.

**LogSNR intervals** Another change with respect to SiD2 is that we set guidance intervals in terms  $t$ . Here we evaluate the usual setting in terms of logSNR, which performs worse.

**GT spectrum (oracle)** We quantify the effect of sampling the power spectrum parameters, by evaluating a model with the spectrum computed from ground truth images. Results are close, showing no loss when using the RAPSD sampler.

## 6. Conclusion and limitations

This work demonstrated that more efficient diffusion noise schedules can be obtained by leveraging the image power spectrum and specializing the schedule for each instance. Our results showed improved quality over strictly single-stage pixel diffusion models, while needing fewer denoising

Table 2. Ablation studies on ImageNet  $256 \times 256$  using the *small* model architecture. We analyze the impact of the our main contributions, including scheduling, conditioning mechanisms, and guidance interval parametrization.

METHOD	NFE	FID ↓	IS ↑
<i>Baselines</i>			
SiD2 BASELINE	512	1.68	288.2
<b>OURS (MIXED SCHEDULE)</b>	256	1.42	297.0
<i>Schedule Design</i>			
FIXED SCHEDULE (MEDIAN)	256	1.61	299.3
COSINE WITH MINMAX	256	1.98	271.4
FREQUENCY-FOCUSED ONLY	256	5.16	178.7
POWER-FOCUSED ONLY	256	5.18	316.2
<i>Conditioning &amp; Sampling</i>			
W/O MINMAX CONDITIONING	256	1.58	302.8
LOGSNR INTERVALS	256	1.58	287.7
GT SPECTRUM (ORACLE)	256	1.43	298.2

steps, though they generally lag behind state-of-the-art latent diffusion and distilled models. We leave for future work to investigate whether similar techniques apply to these multi-stage models, noting that Skorokhodov et al. (2025) investigated the differences between latent and RGB spectra. While our noise schedules successfully adapt to different resolutions with no hyperparameter changes, other aspects of the model still need tuning; namely, the loss bias and guidance intervals. It remains to be seen whether these could also be tied to spectral properties.

## Acknowledgments

We are grateful to Emiel Hoogeboom and Leonardo Zepeda-Núñez for reading the manuscript and providing valuable feedback. We also thank the authors of Simpler Diffusion, upon which our method is built.

## References

- Albergo, M. S. and Vanden-Eijnden, E. Building normalizing flows with stochastic interpolants. In *International Conference on Learning Representations (ICLR)*, 2023.
- Benita, R., Elad, M., and Keshet, J. Spectral analysis of diffusion models with application to schedule design. *arXiv preprint arXiv:2502.00180*, 2025.
- Blattmann, A., Rombach, R., Ling, H., Dockhorn, T., Kim, S. W., Fidler, S., and Kreis, K. Align your latents: High-resolution video synthesis with latent diffusion models. In *Proceedings of the IEEE/CVF Conference on Computer Vision and Pattern Recognition (CVPR)*, pp. 22563–22575, 2023.
- Brooks, T., Peebles, B., Holmes, C., DePue, W., Guo, Y., Jing, L., Schnurr, D., Taylor, J., Luhman, T., Luhman, E., Ng, C., Wang, R., and Ramesh, A. Video generation models as world simulators. 2024. URL <https://openai.com/research/video-generation-models-as-world-simulators>.
- Chen, S., Ge, C., Zhang, S., Sun, P., and Luo, P. PixelFlow: Pixel-Space Generative Models with Flow. *arXiv preprint arXiv:2504.07963v1*, 2025.
- Chen, T. On the importance of noise scheduling for diffusion models. *arXiv preprint arXiv:2301.10972*, 2023.
- DeepMind, G. Veo: a text-to-video generation system. Technical report, May 2025. URL <https://storage.googleapis.com/deepmind-media/veo/Veo-3-Tech-Report.pdf>.
- Dieleman, S. Diffusion is spectral autoregression, 2024. URL <https://sander.ai/2024/09/02/spectral-autoregression.html>.
- Dosovitskiy, A., Beyer, L., Kolesnikov, A., Weissenborn, D., Zhai, X., Unterthiner, T., Dehghani, M., Minderer, M., Heigold, G., Gelly, S., Uszkoreit, J., and Houshy, N. An image is worth 16x16 words: Transformers for image recognition at scale. In *International Conference on Learning Representations (ICLR)*, 2021.
- Esser, P., Kulal, S., Blattmann, A., Entezari, R., Müller, J., Saini, H., Levi, Y., Lorenz, D., Sauer, A., Boesel, F., Podell, D., Dockhorn, T., English, Z., and Rombach, R. Scaling rectified flow transformers for high-resolution image synthesis. In *International Conference on Machine Learning (ICML)*, pp. 12606–12633, 2024.
- Falck, F., Pandeva, T., Zahirnia, K., Lawrence, R., Turner, R., Meeds, E., Zazo, J., and Karmalkar, S. A fourier space perspective on diffusion models. *arXiv preprint arXiv:2505.11278*, 2025.
- Field, D. J. Relations between the statistics of natural images and the response properties of cortical cells. *Journal of the Optical Society of America A*, 4(12):2379, 1987.
- Geng, Z., Deng, M., Bai, X., Kolter, J. Z., and He, K. Mean flows for one-step generative modeling. *arXiv preprint arXiv:2505.13447*, 2025.
- Hang, T., Gu, S., Bao, J., Wei, F., Chen, D., Geng, X., and Guo, B. Improved noise schedule for diffusion training. In *Proceedings of the IEEE/CVF International Conference on Computer Vision (ICCV)*, pp. 4796–4806, 2025.
- Hansen-Estruch, P., Yan, D., Chung, C.-Y., Zohar, O., Wang, J., Hou, T., Xu, T., Vishwanath, S., Vajda, P., and Chen, X. Learnings from Scaling Visual Tokenizers for Reconstruction and Generation. *arXiv preprint arXiv:2501.09755v1*, 2025.
- Heusel, M., Ramsauer, H., Unterthiner, T., Nessler, B., and Hochreiter, S. Gans trained by a two time-scale update rule converge to a local nash equilibrium. *Advances in Neural Information Processing Systems (NeurIPS)*, 30, 2017.
- Ho, J. and Salimans, T. Classifier-free diffusion guidance. In *NeurIPS 2021 Workshop on Deep Generative Models and Downstream Applications*, 2021.
- Ho, J., Jain, A., and Abbeel, P. Denoising diffusion probabilistic models. *Advances in Neural Information Processing Systems (NeurIPS)*, 33:6840–6851, 2020.
- Ho, J., Saharia, C., Chan, W., Fleet, D. J., Norouzi, M., and Salimans, T. Cascaded diffusion models for high fidelity image generation. *Journal of Machine Learning Research (JMLR)*, 23(47):1–33, 2022.
- Hoogeboom, E., Heek, J., and Salimans, T. Simple diffusion: end-to-end diffusion for high resolution images. In *International Conference on Machine Learning (ICML)*, 2023.
- Hoogeboom, E., Mensink, T., Heek, J., Lamerigts, K., Gao, R., and Salimans, T. Simpler diffusion: 1.5 fid on imagenet512 with pixel-space diffusion. In *Proceedings of the IEEE/CVF Conference on Computer Vision and Pattern Recognition (CVPR)*, pp. 18062–18071, 2025.

- Huang, X., Salaun, C., Vasconcelos, C., Theobalt, C., Oztireli, C., and Singh, G. Blue noise for diffusion models. In *ACM SIGGRAPH Conference Proceedings*, pp. 1–11, 2024.
- Jabri, A., Fleet, D. J., and Chen, T. Scalable adaptive computation for iterative generation. In *International Conference on Machine Learning (ICML)*, 2023.
- Jiralerspong, T., Earnshaw, B., Hartford, J. S., Bengio, Y., and Scimeca, L. Shaping inductive bias in diffusion models through frequency-based noise control. *arXiv preprint arXiv:2502.10236*, 2025.
- Karras, T., Aittala, M., Aila, T., and Laine, S. Elucidating the design space of diffusion-based generative models. In *Advances in Neural Information Processing Systems (NeurIPS)*, 2022.
- Kingma, D. and Gao, R. Understanding diffusion objectives as the elbo with simple data augmentation. *Advances in Neural Information Processing Systems (NeurIPS)*, 36: 65484–65516, 2023.
- Kingma, D. P., Salimans, T., Poole, B., and Ho, J. Variational diffusion models. *arXiv preprint arXiv:2107.00630*, 2021.
- Kynkäänniemi, T., Karras, T., Laine, S., Lehtinen, J., and Aila, T. Improved precision and recall metric for assessing generative models. In *Advances in Neural Information Processing Systems (NeurIPS)*, pp. 3929–3938, 2019.
- Kynkäänniemi, T., Aittala, M., Karras, T., Laine, S., Aila, T., and Lehtinen, J. Applying guidance in a limited interval improves sample and distribution quality in diffusion models. *Advances in Neural Information Processing Systems (NeurIPS)*, 37:122458–122483, 2024.
- Lee, S., Lin, Z., and Fanti, G. Improving the training of rectified flows. In *Advances in Neural Information Processing Systems (NeurIPS)*, 2024.
- Li, T. and He, K. Back to basics: Let denoising generative models denoise. *arXiv preprint arXiv:2511.13720*, 2025.
- Lin, S., Liu, B., Li, J., and Yang, X. Common diffusion noise schedules and sample steps are flawed. In *Proceedings of the IEEE/CVF Winter Conference on Applications of Computer Vision (WACV)*, pp. 5404–5411, 2024.
- Lipman, Y., Chen, R. T. Q., Ben-Hamu, H., Nickel, M., and Le, M. Flow matching for generative modeling. In *International Conference on Learning Representations (ICLR)*, 2023.
- Liu, X., Gong, C., and Liu, Q. Flow straight and fast: Learning to generate and transfer data with rectified flow. *arXiv preprint arXiv:2209.03003*, 2022.
- Meng, C., Rombach, R., Gao, R., Kingma, D., Ermon, S., Ho, J., and Salimans, T. On distillation of guided diffusion models. In *Proceedings of the IEEE/CVF Conference on Computer Vision and Pattern Recognition (CVPR)*, pp. 14297–14306, 2023.
- Nash, C., Menick, J., Dieleman, S., and Battaglia, P. W. Generating images with sparse representations. In *International Conference on Machine Learning (ICML)*, pp. 7958–7968, 2021.
- Nguyen, T. H. and Tran, A. Swiftbrush: One-step text-to-image diffusion model with variational score distillation. In *Proceedings of the IEEE/CVF Conference on Computer Vision and Pattern Recognition (CVPR)*, pp. 7807–7816, 2024.
- Nichol, A. Q. and Dhariwal, P. Improved denoising diffusion probabilistic models. In *International Conference on Machine Learning (ICML)*, pp. 8162–8171, 2021.
- Perez, E., Strub, F., De Vries, H., Dumoulin, V., and Courville, A. Film: Visual reasoning with a general conditioning layer. *AAAI Conference on Artificial Intelligence*, 2018.
- Podell, D., English, Z., Lacey, K., Blattmann, A., Dockhorn, T., Müller, J., Penna, J., and Rombach, R. SDXL: improving latent diffusion models for high-resolution image synthesis. In *International Conference on Learning Representations (ICLR)*, 2024.
- Ramesh, A., Dhariwal, P., Nichol, A., Chu, C., and Chen, M. Hierarchical text-conditional image generation with CLIP latents. *arXiv preprint arXiv:2204.06125*, 2025.
- Rissanen, S., Heinonen, M., and Solin, A. Generative modelling with inverse heat dissipation. In *International Conference on Learning Representations (ICLR)*, 2023.
- Rombach, R., Blattmann, A., Lorenz, D., Esser, P., and Ommer, B. High-resolution image synthesis with latent diffusion models. In *Proceedings of the IEEE/CVF Conference on Computer Vision and Pattern Recognition (CVPR)*, pp. 10684–10695, 2022.
- Saharia, C., Chan, W., Saxena, S., Li, L., Whang, J., Denton, E. L., Ghasemipour, S. K. S., Lopes, R. G., Ayan, B. K., Salimans, T., Ho, J., Fleet, D. J., and Norouzi, M. Photorealistic text-to-image diffusion models with deep language understanding. In *Advances in Neural Information Processing Systems (NeurIPS)*, 2022.
- Sahoo, S., Gokaslan, A., De Sa, C. M., and Kuleshov, V. Diffusion models with learned adaptive noise. *Advances in Neural Information Processing Systems (NeurIPS)*, 37: 105730–105779, 2024.

- Salimans, T. and Ho, J. Progressive distillation for fast sampling of diffusion models. In *International Conference on Learning Representations (ICLR)*, 2022.
- Salimans, T., Goodfellow, I. J., Zaremba, W., Cheung, V., Radford, A., and Chen, X. Improved techniques for training gans. In *Advances in Neural Information Processing Systems (NeurIPS)*, pp. 2226–2234, 2016.
- Salimans, T., Mensink, T., Heek, J., and Hoogeboom, E. Multistep distillation of diffusion models via moment matching. *Advances in Neural Information Processing Systems (NeurIPS)*, 33:6840–6851, 2024.
- Skorokhodov, I., Girish, S., Hu, B., Menapace, W., Li, Y., Abdal, R., Tulyakov, S., and Siarohin, A. Improving the diffusability of autoencoders. In *International Conference on Machine Learning (ICML)*, 2025.
- Sohl-Dickstein, J., Weiss, E., Maheswaranathan, N., and Ganguli, S. Deep unsupervised learning using nonequilibrium thermodynamics. In *International Conference on Machine Learning (ICML)*, pp. 2256–2265, 2015.
- Song, Y., Dhariwal, P., Chen, M., and Sutskever, I. Consistency models. In *International Conference on Machine Learning (ICML)*, pp. 32211–32252, 2023.
- Torralba, A. and Oliva, A. Statistics of natural image categories. *Network: Computation in Neural Systems*, 14(3): 391–412, 2003.
- van der Schaaf, A. and van Hateren, J. Modelling the power spectra of natural images: Statistics and information. *Vision Research*, 36(17):2759–2770, 1996. ISSN 0042-6989. doi: 10.1016/0042-6989(96)00002-8.
- Wang, S., Gao, Z., Zhu, C., Huang, W., and Wang, L. PixNerd: Pixel Neural Field Diffusion. *arXiv preprint arXiv:2507.23268v2*, 2025.
- Yin, T., Gharbi, M., Zhang, R., Shechtman, E., Durand, F., Freeman, W. T., and Park, T. One-step diffusion with distribution matching distillation. In *Proceedings of the IEEE/CVF Conference on Computer Vision and Pattern Recognition (CVPR)*, pp. 6613–6623, 2024.
- Yu, L., Lezama, J., Gundavarapu, N. B., Versari, L., Sohn, K., Minnen, D., Cheng, Y., Gupta, A., Gu, X., Hauptmann, A. G., Gong, B., Yang, M., Essa, I., Ross, D. A., and Jiang, L. Language model beats diffusion - tokenizer is key to visual generation. In *International Conference on Learning Representations (ICLR)*, 2024.
- Yu, Y., Xiong, W., Nie, W., Sheng, Y., Liu, S., and Luo, J. PixelDiT: Pixel Diffusion Transformers for Image Generation. *arXiv preprint arXiv:2511.20645v1*, 2025.
- Zheng, B., Ma, N., Tong, S., and Xie, S. Diffusion Transformers with Representation Autoencoders. *arXiv preprint arXiv:2510.11690v1*, 2025.

## A. Derivation of Noised RAPSD

Here we provide the derivation for Eq. (9). The noised signal is given by  $z_q = \alpha_q x_0 + \sigma_q \epsilon$ . By the linearity of the DFT, the frequency domain representation is:

$$\hat{z}_q(u) = \alpha_q \hat{x}_0(u) + \sigma_q \hat{\epsilon}(u). \quad (25)$$

The power spectral density (PSD)  $P_{z_q}(u) = |\hat{z}_q(u)|^2$  is:

$$P_{z_q}(u) = (\alpha_q \hat{x}_0(u) + \sigma_q \hat{\epsilon}(u)) \overline{(\alpha_q \hat{x}_0(u) + \sigma_q \hat{\epsilon}(u))} \quad (26)$$

$$= \alpha_q^2 |\hat{x}_0(u)|^2 + \sigma_q^2 |\hat{\epsilon}(u)|^2 + \alpha_q \sigma_q 2 \operatorname{Re}(\hat{x}_0(u) \overline{\hat{\epsilon}(u)}). \quad (27)$$

Since the noise  $\epsilon$  has zero mean and is independent of the signal  $x_0$ , the expected cross-term vanishes:  $\mathbb{E}_\epsilon[\hat{x}_0(u) \overline{\hat{\epsilon}(u)}] = 0$ . Taking the expectation over the noise distribution:

$$\mathbb{E}[P_{z_q}(u)] = \alpha_q^2 P_{x_0}(u) + \sigma_q^2 \mathbb{E}[P_\epsilon(u)]. \quad (28)$$

The RAPSD  $\Psi(k)$  averages the power over constant frequency magnitudes. Applying this operator to both sides:

$$\Psi_{z_q}(k) = \alpha_q^2 \Psi_{x_0}(k) + \sigma_q^2 \Psi_\epsilon(k). \quad (29)$$

For standard Gaussian white noise, the spectrum is flat (white), so the expected power is constant across all frequencies. Following the normalization in Eq. (6),  $\Psi_\epsilon(k) = 1$ . Thus:

$$\Psi_{z_q}(k) = \alpha_q^2 \Psi_{x_0}(k) + \sigma_q^2. \quad (30)$$

## B. Closed-form Noise Schedules

Here we derive the closed-form equations for the frequency-focused and power-focused schedules under the assumption that the RAPSD follows a power law:

$$\tilde{\Psi}_{x_0}(k) = \beta k^\alpha, \quad (31)$$

where  $\beta > 0$  and  $\alpha < 0$ . Recall that the noise scaling factor is interpolated as  $\kappa_t = \kappa_{\max}^t \kappa_{\min}^{1-t}$ , so  $\log \kappa_t = t \log \kappa_{\max} + (1-t) \log \kappa_{\min}$ .

### B.1. Frequency-focused Schedule

The frequency mapping is linear:  $\mu_F(t) = N_f + (1 - N_f)t$ . Substituting the power law into the schedule definition (Eq. (17)):

$$\lambda_F(t) = -\log \kappa_t - \log \tilde{\Psi}_{x_0}(\mu_F(t)) \quad (32)$$

$$= -\log \kappa_t - \log(\beta(\mu_F(t))^\alpha) \quad (33)$$

$$= -\log \kappa_t - \log \beta - \alpha \log(N_f + (1 - N_f)t). \quad (34)$$

### B.2. Power-focused Schedule

For the power-focused schedule, we first compute the normalization constant  $Z$  and the CDF  $F(q)$ .

$$Z = \int_1^{N_f} \beta u^\alpha du = \frac{\beta}{\alpha + 1} (N_f^{\alpha+1} - 1). \quad (35)$$

The CDF is given by:

$$F(q) = \frac{1}{Z} \int_1^q \beta u^\alpha du = \frac{\frac{\beta}{\alpha+1} (q^{\alpha+1} - 1)}{\frac{\beta}{\alpha+1} (N_f^{\alpha+1} - 1)} \quad (36)$$

$$= \frac{q^{\alpha+1} - 1}{N_f^{\alpha+1} - 1}. \quad (37)$$

We solve for the inverse CDF  $\mu_P(t) = F^{-1}(1 - t)$ . Letting  $y = 1 - t$ :

$$y = \frac{\mu_P^{\alpha+1} - 1}{N_f^{\alpha+1} - 1}, \tag{38}$$

$$\mu_P^{\alpha+1} = 1 + y(N_f^{\alpha+1} - 1), \tag{39}$$

$$\mu_P(t) = \left(1 + (1 - t)(N_f^{\alpha+1} - 1)\right)^{\frac{1}{\alpha+1}}. \tag{40}$$

Finally, we substitute  $\mu_P(t)$  into Eq. (17),

$$\lambda_P(t) = -\log \kappa_t - \log(\beta \mu_P(t)^\alpha) \tag{41}$$

$$= -\log \kappa_t - \log \beta - \alpha \log \left[ \left(1 + (1 - t)(N_f^{\alpha+1} - 1)\right)^{\frac{1}{\alpha+1}} \right] \tag{42}$$

$$= -\log \kappa_t - \log \beta - \frac{\alpha}{\alpha + 1} \log \left(1 + (1 - t)(N_f^{\alpha+1} - 1)\right). \tag{43}$$

### C. Additional ablations

Here we show ablations for the new hyperparameters introduced by our method. Table 3 shows an evaluation of the minimum and maximum noise scaling factors  $\kappa_{\min}$  and  $\kappa_{\max}$ . Table 4 shows an evaluation of the classifier-free guidance interval.

*Table 3.* Ablation on the scaling factors for the noise limits  $\kappa_{\min}$  and  $\kappa_{\max}$ . Results on ImageNet  $256 \times 256$ , with a *small* model. We adopt  $\kappa_{\min} = 0.2$  and  $\kappa_{\max} = 200$ .

$\kappa_{\min}$	$\kappa_{\max}$	FID ↓	IS ↑
0.2	200	1.42	297.0
0.2	100	1.48	289.8
0.1	200	1.53	291.0
1.0	100	1.58	302.9
0.1	100	1.63	281.0

*Table 4.* Effect of the  $t$ -based classifier-free guidance interval. Results on ImageNet  $256 \times 256$ , with a *flop-heavy* model. We adopt (0.1, 0.45).

GUIDANCE INTERVAL	FID ↓	IS ↑
(0.10, 0.45)	1.32	294.2
(0.05, 0.40)	1.36	286.1
(0.10, 0.40)	1.37	279.2
(0.05, 0.45)	1.38	306.6
(0.15, 0.40)	1.40	270.9
(0.15, 0.50)	1.44	314.1
(0.10, 0.50)	1.50	321.2
(0.05, 0.50)	1.57	327.5

### D. Implementation details

#### D.1. Architecture and training

We build on (Hoogeboom et al., 2025) and follow their architectures and training protocols. In short, the architecture is a U-ViT with initial convolutional layers, downsampling, a Vision Transformer (ViT) (Dosovitskiy et al., 2021), and mirrored for upsampling. The difference between the *small* and *flop-heavy* models is solely the input patch size where the heavy model has all feature maps and sequence lengths four times larger.

The few hyperparameters we introduce in the diffusion model are listed in Table 5.

#### D.2. RAPSD sampler

The additional model and training procedure we introduce is quite simple. We model the distribution of  $\log \tilde{\Psi}_x(1)$  and  $\log \tilde{\Psi}_x(N_f)$  as a mixture of Gaussians with  $C$  components. The RAPSD sampler consists of a single layer mapping the one-hot encoding of the class label to a vector of dimension  $5C$  representing the component weight  $w_c$ , 2D mean  $\mu_c$  and 2D diagonal covariance  $\sigma_c$ . The loss is, then, the negative log-likelihood of  $v(x) = [\log \tilde{\Psi}_x(1), \log \tilde{\Psi}_x(N_f)]^\top$ :

$$\mathcal{L}_{\text{GMM}}(x) = -\log \sum_{k=1}^C w_c \mathcal{N}(v(x); \mu_c, \text{diag}(\sigma_c^2)). \tag{44}$$

## Spectrally-Guided Diffusion Noise Schedules

Table 5. Hyperparameters for different model configurations and resolutions. We list the optimal classifier-free guidance intervals (in terms of  $t$ ), number of sampling steps (NFE), and the scaling factors  $\kappa_{\min}$  and  $\kappa_{\max}$ .

MODEL	RESOLUTION	GUIDANCE INTERVAL	NFE	$\kappa_{\min}$	$\kappa_{\max}$
SMALL	$128 \times 128$	(0.15, 0.40)	160	0.2	200
HEAVY	$128 \times 128$	(0.15, 0.35)	160	0.2	200
SMALL	$256 \times 256$	(0.10, 0.45)	256	0.2	200
HEAVY	$256 \times 256$	(0.10, 0.45)	256	0.2	200
SMALL	$512 \times 512$	(0.05, 0.50)	256	0.2	200
HEAVY	$512 \times 512$	(0.05, 0.50)	320	0.2	200

We train for 100k steps with batch size 128, Adam with learning rate 0.001, and use  $C = 3$  components. We train one sampler for each resolution and apply to all models at that resolution.

### D.3. Metrics

We evaluate our results using standard generative modeling metrics computed on 50k generated samples.

**Fréchet Inception Distance (FID)** (Heusel et al., 2017) measures the distance between the Gaussian approximations to the distributions of Inception-V3 pool3 features of real and generated images. It is the standard metric for assessing both image quality and diversity. We measure it against the ImageNet training set.

**Spatial FID (sFID)** (Nash et al., 2021) is a variant of FID that utilizes spatial features from intermediate mixed-6/7 layers of the Inception network rather than the spatially pooled features.

**Inception Score (IS)** (Salimans et al., 2016) evaluates the distinctness and diversity of generated images based on the entropy of the predicted class distribution (Inception softmax).

**Precision and Recall** (Kynkäänniemi et al., 2019) separately assess fidelity and diversity. Precision measures the fraction of generated images whose Inception-V3 pool3 features are within the  $k$ -nearest neighbors of a real image (fidelity), while recall measures the fraction of real images that are within the  $k$ -nearest neighbors of a generated image (diversity). We use  $k = 3$  and 50,000 examples from ImageNet training set for this metric.

### E. Generated samples

Figure 6 shows samples generated by our *flop-heavy* model trained on ImageNet  $512 \times 512$ .

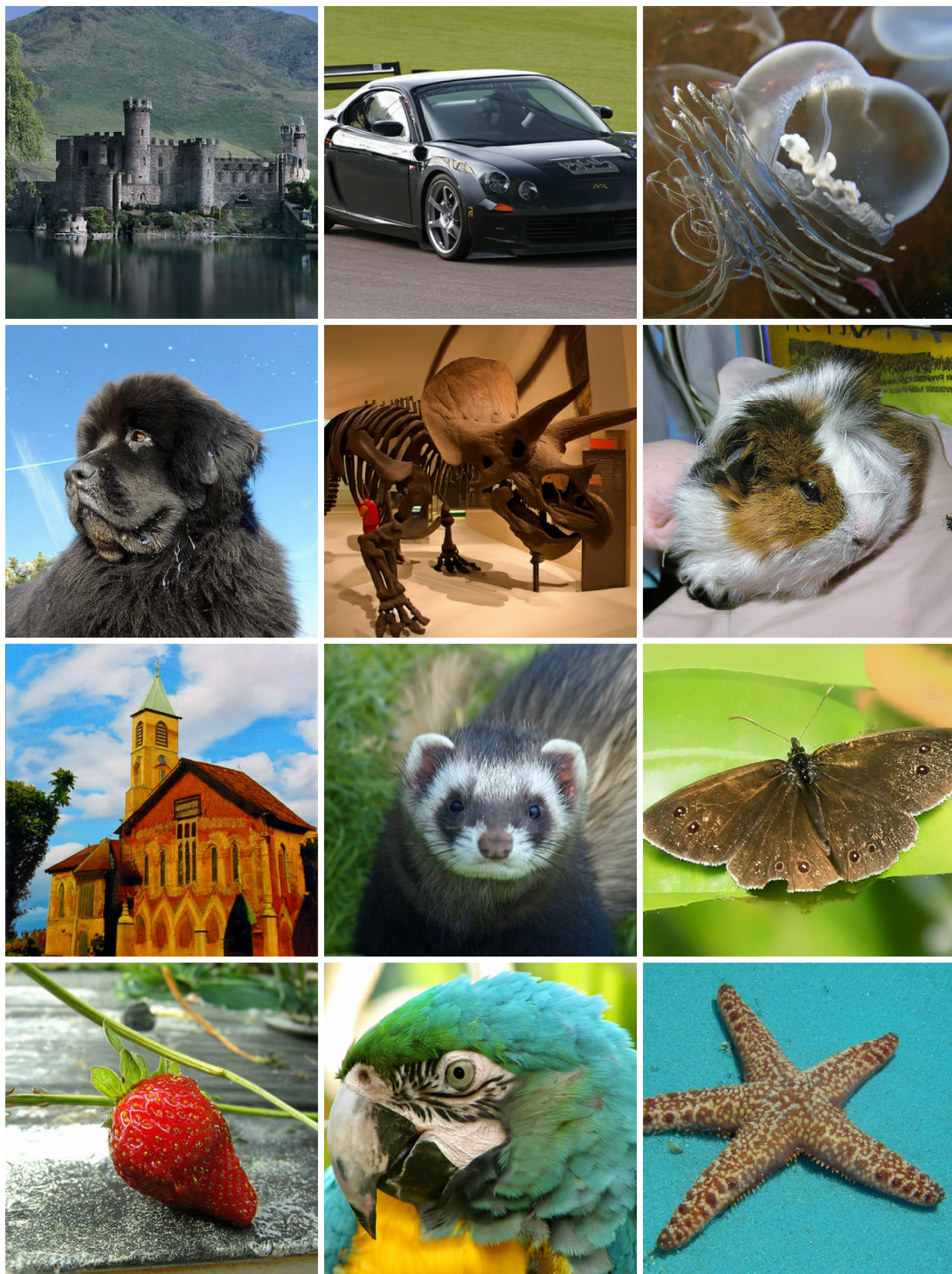


Figure 6. Samples generated by our *flop-heavy* model trained on ImageNet  $512 \times 512$ .